

Post-common envelope binaries from SDSS – XV. Accurate stellar parameters for a cool $0.4 M_{\odot}$ white dwarf and a $0.16 M_{\odot}$ M dwarf in a 3 h eclipsing binary

S. Pyrzas,^{1*} B. T. Gänsicke,¹ S. Brady,² S. G. Parsons,¹ T. R. Marsh,¹ D. Koester,³ E. Breedt,¹ C. M. Copperwheat,¹ A. Nebot Gómez-Morán,⁴ A. Rebassa-Mansergas,⁵ M. R. Schreiber⁵ and M. Zorotovic⁵

¹Department of Physics, University of Warwick, Coventry CV4 7AL

²AAVSO, 5 Melba Drive, Hudson, NH 03051, USA

³Institut für Theoretische Physik und Astrophysik, University of Kiel, 24098 Kiel, Germany

⁴Université de Strasbourg, CNRS, UMR7550, Observatoire Astronomique de Strasbourg, 11 Rue de l'Université, F-67000 Strasbourg, France

⁵Departamento de Física y Astronomía, Facultad de Ciencias, Universidad de Valparaíso, Avenida Gran Bretana 1111, Valparaíso, Chile

Accepted 2011 August 31. Received 2011 August 26; in original form 2011 July 27

ABSTRACT

We identify SDSS J121010.1+334722.9 as an eclipsing post-common-envelope binary, with an orbital period of $P_{\text{orb}} = 2.988$ h, containing a very cool, low-mass, DAZ white dwarf and a low-mass main-sequence star of spectral type M5. A model atmosphere analysis of the metal absorption lines detected in the blue part of the optical spectrum, along with the *Galaxy Evolution Explorer* near-ultraviolet flux, yields a white dwarf temperature of $T_{\text{eff,WD}} = 6000 \pm 200$ K and a metallicity value of $\log [Z/H] = -2.0 \pm 0.3$. The Na I $\lambda\lambda 8183.27, 8194.81$ absorption doublet is used to measure the radial velocity of the secondary star, $K_{\text{sec}} = 251.7 \pm 2.0$ km s⁻¹, and Fe I absorption lines in the blue part of the spectrum provide the radial velocity of the white dwarf, $K_{\text{WD}} = 95.3 \pm 2.1$ km s⁻¹, yielding a mass ratio of $q = 0.379 \pm 0.009$. Light-curve model fitting, using the Markov chain Monte Carlo method, gives the inclination angle as $i = (79^{\circ}.05\text{--}79^{\circ}.36) \pm 0^{\circ}.15$, and the stellar masses as $M_{\text{WD}} = 0.415 \pm 0.010 M_{\odot}$ and $M_{\text{sec}} = 0.158 \pm 0.006 M_{\odot}$. Systematic uncertainties in the absolute calibration of the photometric data influence the determination of the stellar radii. The radius of the white dwarf is found to be $R_{\text{WD}} = (0.0157\text{--}0.0161) \pm 0.0003 R_{\odot}$ and the volume-averaged radius of the tidally distorted secondary is $R_{\text{sec,vol.aver.}} = (0.197\text{--}0.203) \pm 0.003 R_{\odot}$. The white dwarf in SDSS J121010.1+334722.9 is a very strong He-core candidate.

Key words: binaries: close – binaries: eclipsing – stars: fundamental parameters – stars: individual: SDSS 121010.1+334722.9 – stars: late-type – white dwarfs.

1 INTRODUCTION

Our understanding of stellar structure and evolution leads to the fundamental prediction that the masses and radii of stars obey certain mass–radius (M – R) relations. The calibration and testing of the M – R relations require accurate and model-independent measurements of stellar masses and radii, commonly achieved with eclipsing binaries (e.g. Andersen 1991; Southworth & Clausen 2007).

Among main-sequence (MS) stars, M dwarfs of low mass ($<0.3 M_{\odot}$) are the most ubiquitous. However, few eclipsing low-mass MS+MS binaries are known (e.g. López-Morales 2007;

Morales et al. 2009; Çakırlı & Ibanoglu 2010; Dimitrov & Kjurkchieva 2010; Irwin et al. 2010 and references therein) and have accurate measurements of their masses and radii, affecting the calibration of the low-mass end of the MS M – R relation. To further complicate matters, existing measurements consistently result in radii up to 15 per cent larger and effective temperatures 400 K or more below the values predicted by theory (e.g. Ribas 2006; López-Morales 2007). This is not only the case for low-mass MS+MS binaries (Bayless & Orosz 2006), but it is also present in field stars (Berger et al. 2006; Morales, Ribas & Jordi 2008) and the host stars of transiting extrasolar planets (Torres 2007).

The situation is similar for white dwarfs (WDs), the most common type of stellar remnant. Very few WDs have model-independent measurements of their masses and radii (see Parsons et al. 2010a),

*E-mail: s.pyrzas@warwick.ac.uk

and eclipsing WD+WD binaries have only recently been discovered (Steinfadt et al. 2010; Brown et al. 2011; Parsons et al. 2011). Consequently, the finite temperature $M-R$ relation of WDs (e.g. Wood 1995; Panei, Althaus & Benvenuto 2000) remains largely untested by observations (Provencal et al. 1998).

An alternative approach leading to accurate mass and radius measurements for WDs and MS stars is the study of eclipsing WD+MS binaries. Until recently, the population of eclipsing WD+MS binaries had stagnated with only seven systems known (see Pyrzas et al. 2009, for a list), a direct result of the small number of the entire WD+MS binaries sample (~ 30 systems; Schreiber & Gänsicke 2003).

However, in recent years, progress has been made thanks to the Sloan Digital Sky Survey (SDSS; York et al. 2000). A dedicated search for WD+MS binaries contained in the spectroscopic SDSS Data Release 6 (DR6; Adelman-McCarthy et al. 2008) and Data Release 7 (DR7; Abazajian et al. 2009) yielded more than 1600 systems (e.g. Rebassa-Mansergas et al. 2010), of which $\sim 1/3$ are (short-period) post-common-envelope binaries (PCEBs; Schreiber et al. 2008). The majority of these PCEBs contain low-mass, late-type M dwarfs (Rebassa-Mansergas et al. 2010), while a large percentage of the WD primaries are of low mass as well (Rebassa-Mansergas et al. 2011).

A significant fraction of eclipsing systems should exist among this sample of PCEBs. Identifying and studying these eclipsing systems will substantially increase the observational constraints on the $M-R$ relation of both WDs and MS stars. Therefore, we have begun the first dedicated search for eclipsing WD+MS binaries in the SDSS, and five new systems have already been published (Nebot Gómez-Morán et al. 2009; Pyrzas et al. 2009, but see also Drake et al. 2010 for a complementary sample).

SDSS J121010.1+334722.9 (henceforth SDSS 1210), the subject of this paper, is one of the new systems identified in this search. In what follows, we present our observations (Section 2), determine the orbital period and ephemeris (Section 3) and analyse the spectrum of the WD (Section 4). Radial velocity measurements (Section 5) combined with light-curve fitting (Section 6) lead to the determination of the masses and radii of the binary components (Section 7). We also explore the past and future evolution of the system (Section 8).

2 TARGET INFORMATION, OBSERVATIONS AND REDUCTIONS

SDSS 1210 was discovered by Rebassa-Mansergas et al. (2010) as a WDMS binary dominated by the flux of a low-mass companion with a spectral type M5V, suggesting that the WD must be very cool. Inspecting the Na I $\lambda\lambda 8183.27, 8194.81$ doublet in the six SDSS subspectra¹ with exposure times of 15–30 min taken over the course of three nights, we found large radial velocity variations that strongly suggested an orbital period of a few hours. We obtained time-series photometry of SDSS 1210 with a 16-inch telescope equipped with an ST8-XME CCD camera, with the aim to measure the orbital period from the expected ellipsoidal modulation, and immediately detected a shallow eclipse in the light curve. Enticed by this discovery, we scheduled SDSS 1210 for additional high-time resolution photometry, using RISE on the Liverpool Telescope (LT), with which a total of nine eclipses were observed.

¹ The subexposures that are co-added to produce one SDSS spectrum of a given object.

Table 1. SDSS coordinates and u, g, r, i, z magnitudes of the target SDSS 1210 and the comparison stars used in the analysis. We also provide the GALEX NUV magnitude of SDSS 1210.

Star	RA	Dec.	u	g	r	i	z	NUV
T	182.54221	33.78969	18.10	16.94	16.16	14.92	14.02	20.821
C1	182.55470	33.76832	17.72	15.98	15.33	15.11	15.02	
C2	182.54229	33.73406	19.95	17.33	16.01	15.33	14.94	
C3	182.62616	33.78141	16.85	15.80	15.46	15.34	15.34	

Table 1 lists the SDSS coordinates and magnitudes of SDSS 1210 and the three comparison stars used in the analysis presented in this paper, while Table 2 summarizes our photometric and spectroscopic observations. We note that SDSS 1210 has a *Galaxy Evolution Explorer* (GALEX; Morrissey et al. 2007) near-ultraviolet (NUV) detection, but no far-ultraviolet (FUV) detection.

2.1 Photometry: LT/RISE

Photometric observations were obtained with the robotic 2.0-m LT on La Palma, Canary Islands, using the high-speed frame-transfer CCD camera RISE (Steele et al. 2004) equipped with a single wideband $V + R$ filter (Steele et al. 2008). Observations were carried out in 1-h blocks, using a 2×2 binning mode with exposure times of 5 s.

The data were de-biased and flat-fielded in the standard fashion within the LT reduction pipeline and aperture photometry was performed using SExtractor (Bertin & Arnouts 1996) in the manner described in Gänsicke et al. (2004).

A sample light curve is shown in Fig. 1. The out-of-eclipse variation is ellipsoidal modulation, arising from the tidally deformed secondary.

2.2 Spectroscopy: WHT/ISIS

Time-resolved spectroscopy was carried out at the 4.2-m William Herschel Telescope (WHT) on La Palma, Canary Islands, equipped with the double-armed Intermediate dispersion Spectrograph and Imaging System (ISIS). The spectrograph was used with a 1-arcsec slit, and an 600 lines mm^{-1} grating (R600B/R600R) on each of the blue and red arms, although a few spectra were obtained with a 1200 lines mm^{-1} grating on the red arm (R1200R). Both the EEV12 CCD on the blue arm and the REDPLUS CCD on the red arm were binned by three in the spatial direction and two in the spectral direction. This set-up resulted in an average dispersion of 0.88 Å per binned pixel over the wavelength range 3643–5137 Å (blue arm) and 0.99 Å per binned pixel over the wavelength range 7691–9184 Å (red arm, R600R). From measurements of the full width at half-maximum of arc-lines and strong skylines, we determine the resolution to be 1.4 Å.

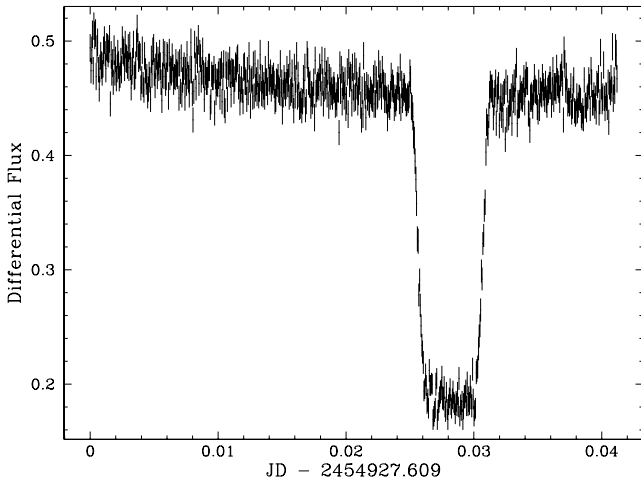
The spectra were reduced using the Starlink² packages KAPPA and FIGARO and then optimally extracted (Horne 1986) using the PAMELA³ code (Marsh 1989). The wavelength scale was derived from copper–neon and copper–argon arc lamp exposures taken every hour during the observations, which we interpolated to the middle of each of the science exposures. For the blue arm the calibration was determined from a fifth-order polynomial fit to 25 lines, with a root mean square

² Maintained and developed by the Joint Astronomy Centre and available from <http://starlink.jach.hawaii.edu/starlink>

³ Available from <http://www.warwick.ac.uk/go/trmarsh>

Table 2. Log of the photometric and spectroscopic observations. For the LT observations, we also provide the number of 1-h observing blocks per night.

Date	Telescope	Filter/grating	Exp. (s)	Blocks	Frames	Eclipses
2009 April 01	LT	V+R	5	1	708	1
2009 April 02	LT	V+R	5	2	1416	0
2009 April 03	LT	V+R	5	2	1416	1
2009 April 04	LT	V+R	5	2	1416	1
2009 April 05	LT	V+R	5	3	2124	1
2009 April 06	LT	V+R	5	1	708	0
2009 April 29	WHT	R600B/R1200R	900	–	1	–
2009 May 02	WHT	R600B/R1200R	900	–	3	–
2010 April 23	WHT	R600B/R1200R	600	–	1	–
2010 May 18	WHT	R600B/R600R	900	–	12	–
2011 February 06	LT	V+R	5	1	720	1
2011 March 02	LT	V+R	5	1	720	1
2011 April 02	LT	V+R	5	1	720	1
2011 May 08	LT	V+R	5	1	720	1
2011 July 03	LT	V+R	5	1	720	1

**Figure 1.** Sample light curve of SDSS 1210 obtained with a 5-s cadence using RISE on the LT on 2009 April 05.

(rms) of 0.029 \AA . The red arm was also fitted with a fifth-order polynomial, to 17 arclines. The rms was 0.032 \AA .

3 ORBITAL PERIOD AND EPHEMERIS

We determined the orbital period and ephemeris of SDSS 1210 through mid-eclipse timings. This was achieved as follows.

Mid-eclipse times were measured by mirroring the observed eclipse profile around an estimate of the eclipse centre and shifting the mirrored profile against the original until the best overlap was found. This method is particularly well suited for the box-shaped eclipse profiles in (deeply) eclipsing PCEBs.

An initial estimate of the cycle count was then obtained by fitting eclipse phases $(\phi_0^{\text{observed}} - \phi_0^{\text{fit}})^{-2}$ over a wide range of trial periods. Once an unambiguous cycle count was established, a linear fit, of the form $T = T_0 + P_{\text{orb}} E$, was performed to the times of mid-eclipse versus cycle count, yielding a preliminary orbital ephemeris.

Subsequently, we phase folded our data set using this preliminary ephemeris and proceeded with the light-curve model fitting (see Section 6). Having an accurate model at hand, we refitted each light curve individually. This provides a robust estimate of the error on

Table 3. Times of mid-eclipse (and their errors), O–C values (and their errors) and cycle number for the ephemeris of SDSS 1210. Mid-eclipse times and errors are in MJD(BTDB), O–C values and errors are in seconds.

Mid-eclipse (d)	Error (d)	O–C (s)	Error (s)	Cycle
54923.0336744	0.0000060	–1	1	0
54925.0255324	0.0000082	1	1	16
54926.1459281	0.0000069	–0	1	25
54927.1418460	0.0000087	–0	1	33
55599.1376175	0.0000061	3	1	5431
55623.0396100	0.0000056	–1	1	5623
55654.0375754	0.0000081	–0	1	5872
55690.0151216	0.0000063	1	1	6161
55745.9109933	0.0000069	–2	1	6610

the mid-eclipse time, as our code includes the time of mid-eclipse T_0 as a free parameter.

Repeating the cycle count determination and the linear ephemeris fitting, as described above, we obtain the following ephemeris for SDSS 1210:

$$\text{MJD (BTDB)} = 54923.033\,686(6) + 0.124\,489\,764(1) E, \quad (1)$$

calculated on a Modified Julian Date-time-scale and corrected to the Solar system barycentre, with the numbers in parentheses indicating the error on the last digit. Thus, SDSS 1210 has an orbital period of $P_{\text{orb}} = 2.987\,754\,336(24) \text{ h}$. The mid-eclipse times, the observed minus calculated values (O–C) and their respective errors are given in Table 3. Given the short baseline, there is as yet no evidence for period changes which are frequently seen in such binaries (e.g. Parsons et al. 2010b).

4 SPECTROSCOPIC ANALYSIS

Although the SDSS spectrum of SDSS 1210 remained inconclusive with respect to the nature of the WD (Rebassa-Mansergas et al. 2010), our blue-arm WHT spectroscopy immediately revealed a host of narrow metal lines that exhibit radial velocity variations antiphased with respect to those of the M dwarf. The WHT spectra obtained in 2010 May, averaged in the WD rest frame and continuum normalized, are shown in Fig. 2 and illustrate the wealth of absorption lines from Mg, Al, Si, Ca, Mn and Fe. Similar metal

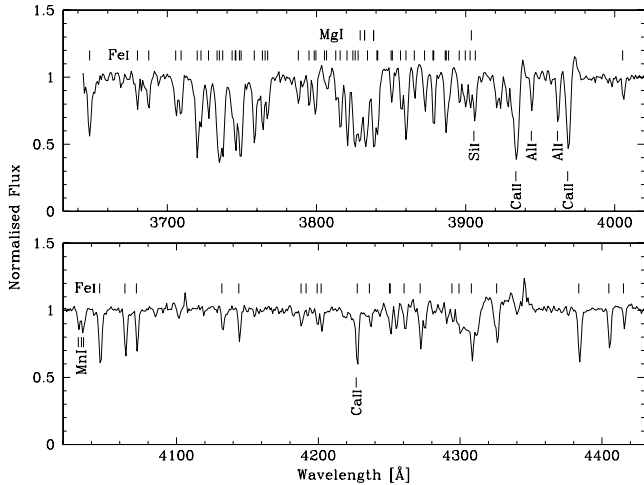


Figure 2. The normalized average WHT spectrum in the WD rest frame, along with line identifications for absorption lines originating in the WD photosphere.

lines have been detected in the optical spectra of a few other cool PCEBs, e.g. RR Cae (Zuckerman et al. 2003) or LTT 560 (Tappert et al. 2007), and indicate accretion of mass via a wind from the M dwarf.

We have analysed the blue WHT spectra using hydrogen dominated but metal-polluted (DAZ) spectra calculated with the stellar atmosphere code described by Koester (2010). We fixed the surface gravity to $\log g = 7.70$, as determined from the fits to the LT light curve (Section 6). The model grid covered effective temperatures $5400 \leq T_{\text{eff,WD}} \leq 7400$ K in steps of 200 K and metal and He abundances of $\log [Z/H] = -3.0, -2.3, -2.0, -1.3, -1.0$, with all relevant elements up to zinc included, and fixed their relative abundances ratios to the respective solar values. We then fitted the model spectra to the average WHT spectrum in the range 3645–3930 Å, where the contribution of the M dwarf is entirely negligible. A good fit is found for $T_{\text{eff,WD}} \simeq 6000$ K and metal abundances at $\simeq 0.01$ their solar values, however, the effective temperature and the metal abundances are strongly correlated (Fig. 3).

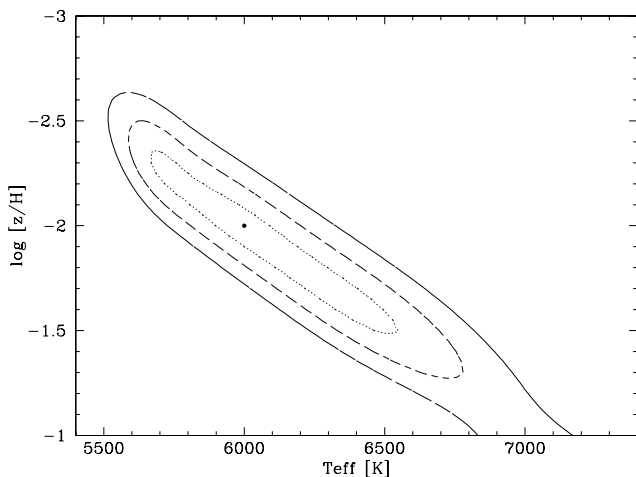


Figure 3. Results of model spectra fitting to the average WHT spectrum. The single, big point indicates the best-fitting solution. The contours indicate the regions where the χ^2 of the fit is within 1, 2 and 3σ (dotted, short-dashed and long-dashed lines, respectively) of the minimum (single point).

This degeneracy is lifted by including the *GALEX* detection of SDSS 1210, as the predicted NUV flux is a strong function of the effective temperature. The uncertainty in the absolute flux calibrations of our WHT spectra and the *GALEX* observations introduces a small systematic uncertainty on the final result, and we settle for $T_{\text{eff,WD}} = 6000 \pm 200$ K and $\log [Z/H] = -2.0 \pm 0.3$. Independently, the weakness of the Balmer lines in the WHT spectrum also requires that $T_{\text{eff,WD}} \lesssim 6400$ K. The spectral modelling of SDSS 1210 is illustrated in Fig. 4.

Adopting the WD radius from the light-curve fit (Sections 6 and 7), $R_{\text{WD}} = 0.0159 R_{\odot}$, the flux-scaling factor of the best-fitting spectral model implies a distance of $d \simeq 50 \pm 5$ pc, which is in good agreement with $d \sim 66 \pm 34$ pc estimated by Rebassa-Mansergas et al. (2010) from fitting the M dwarf.

The detection of metals in the photosphere of the WD allows an estimate of the accretion rate (e.g. Dupuis et al. 1993; Koester & Wilken 2006), as long as the system is in accretion–diffusion equilibrium. In cool, hydrogen-rich atmospheres, such as the one in SDSS 1210, the diffusion time-scales of the different metals detected in the WHT spectrum vary by a factor of ~ 2 for a given temperature, and are, for $T_{\text{eff,WD}} = 6000$ K, in the range 30 000–60 000 yr.⁴ It is plausible to assume that the average accretion rate over the diffusion time-scales involved is constant, as the binary configuration (separation of the two stars, Roche lobe filling factor of the companion) changes on much longer time-scales. Summing up the mass fluxes at the bottom of the convective envelope, and taking into account the uncertainties in $T_{\text{eff,WD}}$ and the metal abundances, gives $\dot{M} \simeq (5 \pm 2) \times 10^{-15} M_{\odot} \text{ yr}^{-1}$. There are now three PCEBs with similar stellar components that have measured accretion rates: RR Cae ($\dot{M} \simeq 4 \times 10^{-16} M_{\odot} \text{ yr}^{-1}$; Debes 2006); LTT 560 ($\dot{M} \simeq 5 \times 10^{-15} M_{\odot} \text{ yr}^{-1}$; Tappert et al. 2011) and SDSS 1210 ($\dot{M} \simeq 5 \times 10^{-15} M_{\odot} \text{ yr}^{-1}$).

Although SDSS 1210 and LTT 560 have similar orbital periods, the period of RR Cae is roughly twice as long, suggesting that the efficiency of wind accretion decreases as the binary separation and Roche lobe size of the companion increase, as is expected. A more systematic analysis of the wind-loss rates of M dwarfs and the efficiency of wind accretion in close binaries would be desirable, but will require a much larger sample of systems.

5 THE SPECTROSCOPIC ORBIT

Radial velocities of the binary components have been measured from the Fe I $\lambda\lambda 4045.813, 4063.594, 4071.737, 4132.058, 4143.869$ absorption lines for the WD and the Na I $\lambda\lambda 8183.27, 8194.81$ absorption doublet for the secondary star.

The Fe I lines were simultaneously fitted with a second-order polynomial plus five Gaussians of common width and a separation fixed to the corresponding laboratory values. A sine fit to the radial velocities phase folded using the orbital ephemeris (equation 1) yields $K_{\text{WD}} = 95.3 \pm 2.1 \text{ km s}^{-1}$ and $\gamma_{\text{WD}} = 24.2 \pm 1.4 \text{ km s}^{-1}$.

The Na I doublet was fitted with a second-order polynomial plus two Gaussians of common width and a separation fixed to the corresponding laboratory value. A sine fit to the radial velocities phase

⁴ For completeness, we note that because we have adopted solar abundance ratios for the metals, these small differences in diffusion time-scales imply slightly non-solar ratios in the accreted material. In principle, the individual metal-to-metal ratios can be determined from the observed spectrum of the WD, and hence allow us to infer the abundances of the companion star, however, this requires data with substantially higher spectral resolution to resolve the line blends.

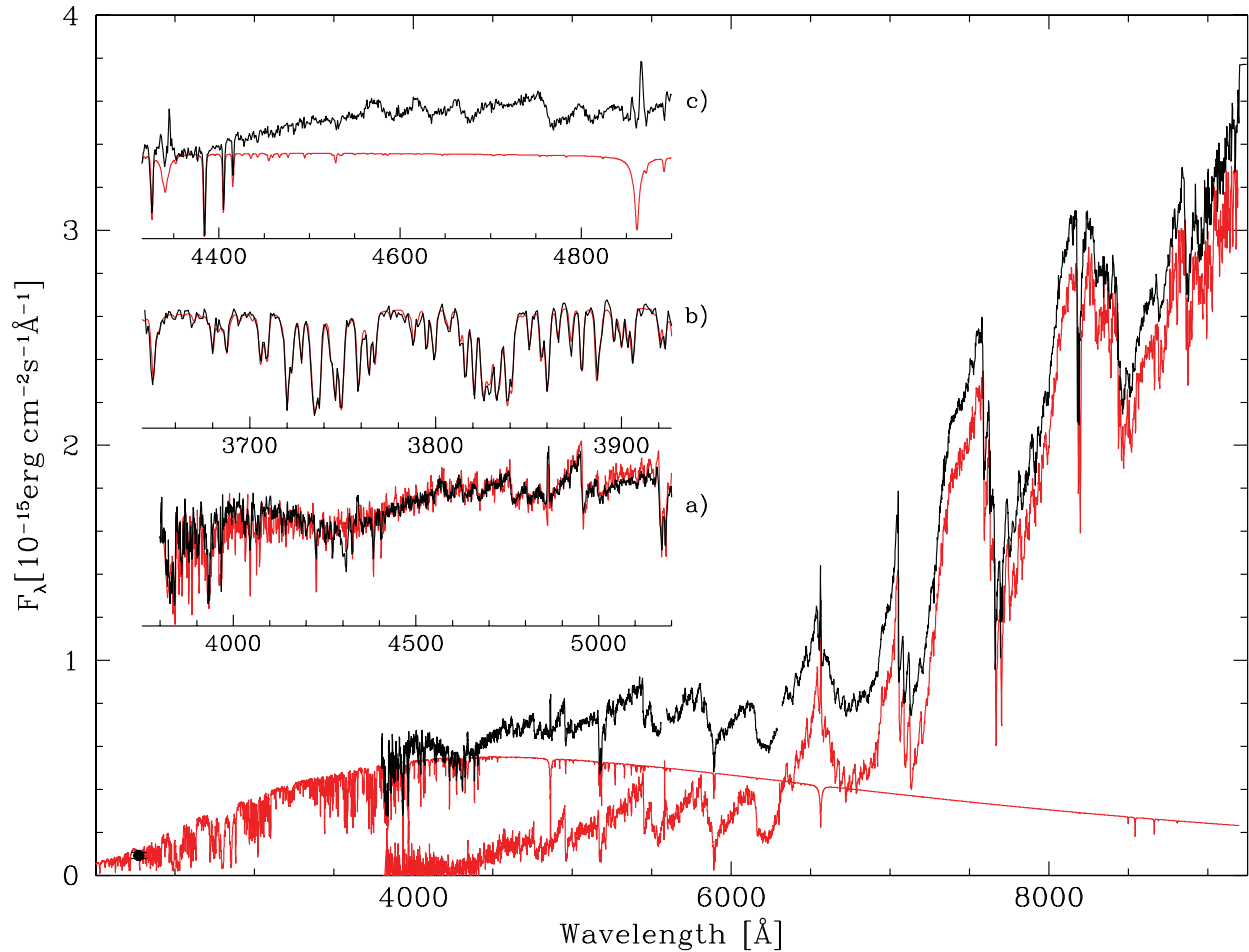


Figure 4. Spectral modelling of SDSS 1210. Main panel: the SDSS spectrum (black) and the *GALEX* NUV flux (black point), along with the best-fitting WD model (red*, $T_{\text{eff,WD}} = 6000$ K, $\log g = 7.70$, $\log [Z/H] = -2.0$) and the best-fitting M-dwarf template for the companion (red*, spectral type M5). Inset (a): the sum of the WD model and M-dwarf template provide a good match to the blue end of the SDSS spectrum (black), with the low flux of the M-dwarf template being the dominant limitation. Inset (b): best-fitting WD model (red*) and the average WHT spectrum for $\lambda < 3930$ Å, where the M dwarf contributes practically nothing to the observed flux. Inset (c): best-fitting WD model (red*) and the average WHT spectrum (black) illustrating the weakness of the $H\beta$ and $H\gamma$ lines of the WD. Increasing the temperature very rapidly results in Balmer lines and/or a NUV flux that are inconsistent with the observations. *The coloured figure is available in the online version only.

folded using the orbital ephemeris yields $K_{\text{sec}} = 251.7 \pm 2.0$ km s $^{-1}$ and $\gamma_{\text{sec}} = 12.2 \pm 0.9$ km s $^{-1}$.

Fig. 5 shows the measured radial velocities phase folded on the orbital period and the corresponding sine fits.

Knowledge of both radial velocities allows us to obtain the mass ratio q of the binary, namely $q = K_{\text{WD}}/K_{\text{sec}} = 0.379 \pm 0.009$. We tentatively interpret the difference between γ_{WD} and γ_{sec} as the gravitational redshift of the WD $z_{\text{WD,spec}}$, which yields $z_{\text{WD,spec}} = 11.9 \pm 1.7$ km s $^{-1}$ (see also Section 7).

6 LIGHT-CURVE MODELLING

To obtain the stellar parameters of the binary components, light-curve models were fitted to the data using *LCURVE* (see Copperwheat et al. 2010 for a description, as well as Pyrzas et al. 2009; Parsons et al. 2010a, 2011 for further applications).

6.1 Code input

The code computes a model based on input system parameters supplied by the user. The physical parameters defining the models

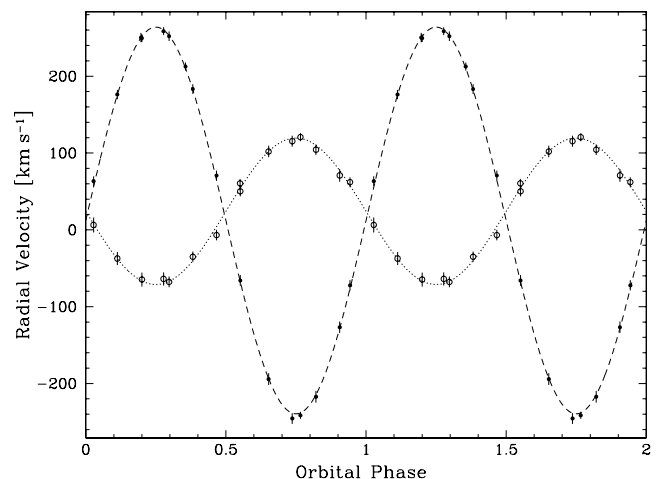


Figure 5. Phase-folded radial velocity curves of the secondary star (filled circles) and the WD (open circles), with their respective errors. Also shown are the sine fits to the velocities of both components. A full cycle is repeated for clarity.

are (i) the mass ratio $q = M_{\text{sec}}/M_{\text{WD}}$, (ii) the binary inclination i , (iii) the stellar radii scaled by the binary separation $r_{\text{WD}} = R_{\text{WD}}/a$ and $r_{\text{sec}} = R_{\text{sec}}/a$, (iv) the unirradiated stellar temperatures $T_{\text{eff,WD}}$ and T_{sec} , (v) the sum of the unprojected stellar orbital speeds $V_S = (K_{\text{WD}} + K_{\text{sec}})/\sin i$, (vi) the time of mid-eclipse of the WD T_0 , (vii) limb- and gravity-darkening coefficients and (viii) the distance d . The code accounts for the distance simply as a scaling factor that can be calculated very rapidly for any given model, and so it does not enter the optimization process. All other parameters can be allowed to vary during the fit.

6.2 Free and fixed parameters

During the minimization, we kept $T_{\text{eff,WD}}$ fixed at $T_{\text{eff,WD}} = 6000$ K. The gravity darkening of the secondary was also kept fixed at 0.08 (the usual value for a convective atmosphere). Limb-darkening coefficients were also held fixed. For the WD we calculated quadratic limb-darkening coefficients from a WD model with $T_{\text{eff,WD}} = 6000$ K and $\log g = 7.70$, folded through the RISE filter profile. The corresponding values were found to be $a = 0.174$ and $b = 0.421$ for $I(\mu)/I(1) = 1 - a(1 - \mu) - b(1 - \mu)^2$, with μ being the cosine of the angle between the line of sight and the surface normal. For the secondary star we used the tables of Claret & Bloemen (2011). We interpolated between the values of V and R for a $T = 3000$ K and $\log g = 5$ star, to obtain quadratic limb-darkening coefficients $a' = 0.62$ and $b' = 0.273$. All other parameters were allowed to vary.

6.3 Minimization

Initial minimization is achieved using the downhill-simplex and Levenberg–Marquardt methods (Press 2002), while the Markov chain Monte Carlo (MCMC) method (Press et al. 2007) was used to determine the distributions of our model parameters (e.g. Ford 2006, and references therein).

The MCMC method involves making random jumps in the model parameters, with new models being accepted or rejected according to their probability computed as a Bayesian posterior probability (the probability of the model parameters, θ , given the data, D , $P(\theta|D)$). $P(\theta|D)$ is driven by a combination of χ^2 and a prior probability, $P(\theta)$, that is based on previous knowledge of the model parameters.

In our case, the prior probabilities for most parameters are assumed to be uniform. The photometric data provide constraints for the radii and inclination angle, however, the photometry alone cannot constrain the masses, as the light curve itself is only weakly dependent on q . To alleviate this, we can use our knowledge of K_{WD} and K_{sec} . At each jump, the model values K_{WD}^m and K_{sec}^m are calculated through q , i and V_S . $P(\theta)$ is then evaluated on the basis of the observed K_{WD} and K_{sec} , assuming a Gaussian prior probability $P(\mu, \sigma^2)$, with μ and σ corresponding to the measured values and errors of K_{WD} and K_{sec} .

A crucial practical consideration of MCMC is the number of steps required to fairly sample the parameter space, which is largely determined by how closely the distribution of parameter jumps matches the true distribution. We therefore built up an estimate of the correct distribution starting from uncorrelated jumps in the parameters, after which we computed the covariance matrix from the resultant chain of parameter values. The covariance matrix was then used to define a multivariate normal distribution that was used to make the jumps for the next chain. At each stage the actual size of the jumps was scaled by a single factor set to deliver a

model acceptance rate of ≈ 25 per cent (Roberts, Gelman & Gilks 1997). After three such cycles, the covariance matrix showed only small changes, and at this point we carried out the long ‘production runs’ during which the covariance and scalefactor which define the parameter jumps were held fixed.

6.4 Stellar parameters

Using the following set of equations, the stellar and binary parameters are obtained directly from the posterior distribution of the model parameters, as output from the MCMC minimization.

The binary separation is obtained from the model parameter V_S through

$$a = \frac{P_{\text{orb}}}{2\pi} V_S. \quad (2)$$

The WD and secondary masses are obtained from the model parameters q and V_S as

$$M_{\text{WD}} = \frac{P_{\text{orb}}}{2\pi G} \frac{1}{1+q} V_S^3 \quad (3)$$

and

$$M_{\text{sec}} = \frac{P_{\text{orb}}}{2\pi G} \frac{q}{1+q} V_S^3. \quad (4)$$

The stellar radii are directly obtained from the model parameters r_{WD} and r_{sec} and equation (2) and the surface gravity of the WD is of course given by

$$\log g = \log \left(\frac{GM_{\text{WD}}}{R_{\text{WD}}^2} \right). \quad (5)$$

6.5 Intrinsic data uncertainties

The acquisition of high-precision absolute photometry on the LT in service mode is somewhat difficult to achieve. Each observing block individually covered only a third of the orbital phase and the blocks were obtained over many nights, under varying conditions (seeing, sky brightness, extinction, airmass). The data are sensitive to changes in conditions, as they have been obtained through the very broad and non-standard $V + R$ filter of RISE. In the absence of a flux standard, the photometry cannot be calibrated in absolute terms. When phase folding the LT data, significant scatter is found at orbital phases where individual observing blocks with discrepant calibrations contribute. This affects both the shape of the eclipse, mainly the steepness of the WD ingress/egress and, to a lesser extent, the eclipse duration, and the out-of-eclipse variation, i.e. the profile of the ellipsoidal modulation. As a result, there is an unavoidable systematic uncertainty in the photometric accuracy of our data, which will influence the determination of the stellar parameters.

To gauge the effect of the systematic uncertainties we worked in the following fashion: each observing block has been reduced thrice, each time using one of the three comparison stars reported in Table 1. C1 has a $g - r$ colour index comparable to SDSS 1210, C2 is fairly red, while C3 is fairly blue. The data of each reduction were then phase folded together and two light curves were produced: one containing all the photometric points and one where (2–3) observing blocks with an obviously large intrinsic scattering were omitted. Thus, we ended up with six phase-folded light curves. A dedicated MCMC optimization was calculated for each light curve. We will use the following notation when referring to these chains: C1A denotes a light curve produced with comparison star C1 and all datapoints, C2E denotes a light curve produced with comparison star C2 excluding observing blocks and so on.

7 RESULTS

The results of the six MCMC processes are summarized in Table 4. The quoted values and errors are purely of statistical nature and represent the mean and rms of the posterior distribution of each parameter. The radius of the secondary, as determined by r_{sec} and a , is measured along the line connecting the centres of the two stars

and, due to the tidal distortion, its value is larger than the average radius. Therefore, in Table 4 we also report the more representative value of the volume-averaged radius.

To illustrate the achieved quality of the fits, we plot models C1A and C1E in Fig. 6. While the overall quality of the fit is very satisfactory, the model seems to slightly overpredict the flux at the ‘wings’ of the ellipsoidal modulation profile (phases $\sim 0.05\text{--}0.15$

Table 4. Stellar and binary parameters obtained from MCMC optimization. The quoted values and errors are the mean and rms of the posterior distribution of each parameter. The chains represent light curves created using comparison stars C1, C2 or C3 and either including all (A) observing blocks or excluding (E) those with obviously large scattering. See text for details.

Parameter	C1A	C1E	C2A	C2E	C3A	C3E
q	0.380 ± 0.010	0.380 ± 0.010	0.381 ± 0.010	0.380 ± 0.010	0.378 ± 0.010	0.379 ± 0.010
i ($^\circ$)	79.05 ± 0.15	79.28 ± 0.15	79.03 ± 0.15	79.13 ± 0.15	79.36 ± 0.18	79.29 ± 0.16
M_{WD} (M_\odot)	0.415 ± 0.010	0.414 ± 0.010	0.415 ± 0.010	0.415 ± 0.010	0.414 ± 0.010	0.414 ± 0.010
R_{WD} (R_\odot)	0.0157 ± 0.0003	0.0159 ± 0.0003	0.0161 ± 0.0003	0.0159 ± 0.0003	0.0138 ± 0.0003	0.0150 ± 0.0003
$\text{WD log } g$	7.664 ± 0.015	7.652 ± 0.016	7.641 ± 0.015	7.649 ± 0.017	7.773 ± 0.023	7.700 ± 0.019
M_{sec} (M_\odot)	0.158 ± 0.006	0.157 ± 0.006	0.158 ± 0.006	0.158 ± 0.006	0.156 ± 0.007	0.157 ± 0.006
R_{sec} (R_\odot)	0.217 ± 0.003	0.212 ± 0.003	0.217 ± 0.003	0.215 ± 0.003	0.210 ± 0.004	0.211 ± 0.003
$R_{\text{sec, vol. aver.}}$ (R_\odot)	0.202 ± 0.003	0.199 ± 0.003	0.203 ± 0.003	0.201 ± 0.003	0.197 ± 0.003	0.198 ± 0.003
T_{sec} (K)	~ 2530	~ 2550	~ 2530	~ 2550	~ 2500	~ 2550
Binary separation (R_\odot)	0.871 ± 0.008	0.870 ± 0.008	0.871 ± 0.008	0.871 ± 0.008	0.869 ± 0.008	0.870 ± 0.008

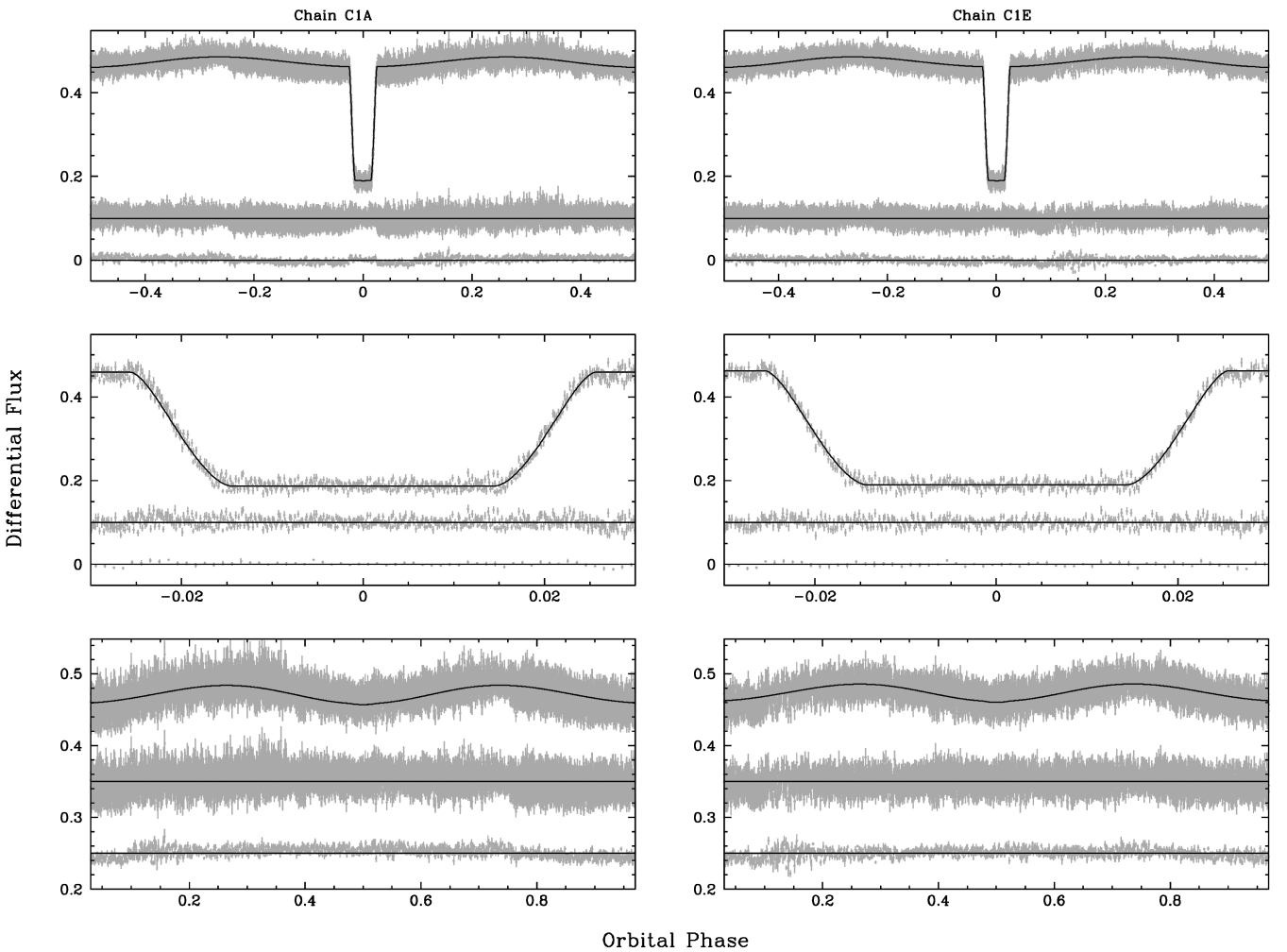


Figure 6. Light-curve fitting results for models C1A (left) and C1E (right). In each of the six panels we plot the phase folded light curve with the model superimposed (top trace), the residuals of the fit (middle trace, offset from 0 for clarity) and a binned version of the residuals (bottom trace). Shown are the entire light curve (top panels), a zoom around the eclipse (middle panels) and the out-of-eclipse ellipsoidal modulation (bottom panels).

and $\sim 0.85\text{--}0.95$). This discrepancy could be data related, due to the intrinsic scattering of points; system related, due to the presence of starspots affecting the modulation; model related, as the treatment of stellar temperatures is based on blackbody spectra, for one specific wavelength; or due to a combination of these factors.

With regard to the binary and stellar parameters, the MCMC results indicate the following: as expected for a detached system, the light curves depend very weakly on q and its value is well constrained by the radial velocities. All six chains give inclination angle values just above 79° , consistent with each other within the errors. There is a slight shift upwards when excluding blocks from the phase folded light curve.

The tight spectroscopic constraints mean that the component masses are largely independent of the model/data set used. Thus, the WD in SDSS 1210 has a mass of $M_{\text{WD}} = 0.415 \pm 0.010 M_\odot$ and the secondary star a mass of $M_{\text{sec}} = 0.158 \pm 0.006 M_\odot$.

The quantity most seriously affected by systematics is the WD radius. This is especially evident when considering models C3A and C3E. However, such a discrepancy is expected, since C3 is considerably bluer than SDSS 1210 and is more susceptible to air-mass/colour effects, leading to large intrinsic scattering. The values for R_{WD} as obtained from C1A, C1E, C2A and C2E are consistent within their errors, indicating a systematic uncertainty comparable to the statistical one. This is illustrated in Fig. 7.

The secondary star radius is affected in a similar, albeit less pronounced, way. All six models lead to values broadly consistent within their statistical errors and a systematic uncertainty of the same order as the statistical one. Fig. 8 shows the six different values of the volume-averaged secondary star radius overplotted on a M – R relation for MS stars. Taken at face value, the results of the MCMC optimization indicate that the secondary is ~ 10 per cent larger than theoretically predicted. As can be seen in Fig. 8, this discrepancy

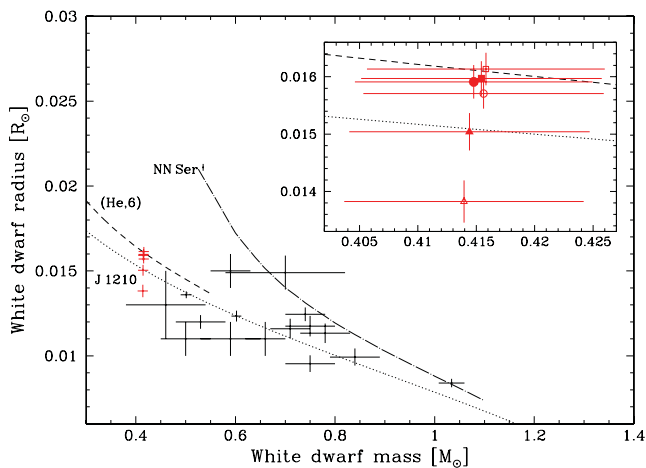


Figure 7. M – R plot for WDs. Black points are data from Provencal et al. (1998), Provencal et al. (2002) and Casewell et al. (2009). The dotted line is the zero-temperature M – R relation of Eggleton as quoted in Verbunt & Rappaport (1988). The dashed line, marked as (He,6) is a M – R relation for a $T_{\text{eff,WD}} = 6000$ K, He-core WD, with a hydrogen layer of $M(\text{H})/M_{\text{WD}} = 3 \times 10^{-4}$, interpolated from the models of Althaus & Benvenuto (1997). NN Ser (Parsons et al. 2010a) is marked, along with the track for $T_{\text{eff,WD}} = 60000$ K, C/O core WD, $M(\text{H})/M_{\text{WD}} = 10^{-4}$ (long dash-dot line), indicating the accuracy achieved in eclipsing PCEBs. The results of the six chains for SDSS 1210 are plotted in red (online version only). Inset panel: zoom-in on the values of SDSS 1210. The points are C1A: open circle; C1E: filled circle; C2A: open square; C2E: filled square; C3A: open triangle; C3E: filled triangle.

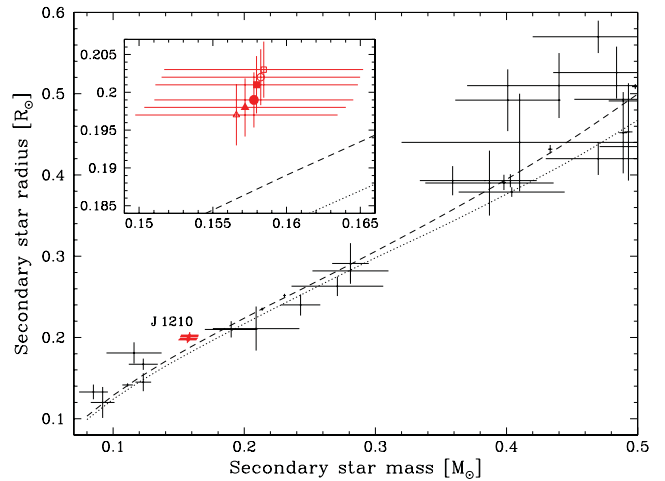


Figure 8. M – R plot for low-mass stars. Black points are data from López-Morales (2007) and Beatty et al. (2007), where the masses of single stars were determined using mass–luminosity relations. The dotted line is the 5.0-Gyr isochrone from Baraffe et al. (1998). The dashed line is a 5.0-Gyr model including effects of magnetic activity from Morales et al. (2010). The results of the six chains for the volume-averaged radius of the secondary in SDSS 1210 are plotted in red (online version only). Inset panel: zoom-in on the values of SDSS 1210. The points are C1A: open circle; C1E: filled circle; C2A: open square; C2E: filled square; C3A: open triangle; C3E: filled triangle.

drops to ~ 5 per cent, if magnetic activity of the secondary is taken into account. With regard to the secondary temperature, we note again that due to the blackbody approximation, the value of T_{sec} does not necessarily represent the true temperature of the star, it is effectively just a flux-scaling factor.

The gravitational redshift predicted by the light-curve models (Table 4), correcting for the redshift of the secondary star, the difference in transverse Doppler shifts and the potential at the secondary star owing to the WD, are $z_{\text{WD}} = 15.9 \pm 0.4 \text{ km s}^{-1}$ from C1E and $z_{\text{WD}} = 15.8 \pm 0.4 \text{ km s}^{-1}$ from C2E, where the errors are purely statistical and have been derived in the same manner as the other quantities reported in Table 4. The systematic uncertainties in our photometric data might still be influencing the result, as the inclination angle and the stellar radii enter the calculation of z_{WD} . Comparing z_{WD} with the spectroscopically determined value of $z_{\text{WD,spec}} = \gamma_{\text{WD}} - \gamma_{\text{sec}} = 11.9 \pm 1.7 \text{ km s}^{-1}$ we find that they are consistent within $\sim 2\sigma$. The systemic velocities γ_{WD} and γ_{sec} are determined from spectroscopic observations obtained using a dual-arm spectrograph, with the WD velocity measured in the blue arm and that of the secondary measured in the red arm (Sections 2 and 5). The observations in both arms are independently wavelength calibrated and the rms of $\sim 0.03 \text{ \AA}$ (Section 2) corresponds to an accuracy of the zero-point of $\sim 1\text{--}2 \text{ km s}^{-1}$. The potential of an offset in the calibrations of the two arms enters the determination of $z_{\text{WD,spec}}$ as an additional systematic uncertainty.

8 PAST AND FUTURE EVOLUTION OF SDSS 1210

Considering its short orbital period, SDSS 1210 must have formed through common-envelope evolution (Paczynski 1976; Webbink 2008; see also Nordhaus et al. 2010 for the additional effects of tidal interaction). As shown by Schreiber & Gänsicke (2003), if the binary and stellar parameters are known, it is possible to

reconstruct the past and predict the future evolution of PCEBs for a given angular momentum loss prescription. Here, we assume classical disrupted magnetic braking (Verbunt & Zwaan 1981). In this context, given the low mass of the secondary, the only angular momentum loss mechanism for SDSS 1210 is gravitational radiation. Based on the temperature and the mass of the WD we interpolate the cooling tracks of Althaus & Benvenuto (1997) and obtain a cooling age of $t_{\text{cool}} = 3.5$ Gyr. This corresponds to the time that passed since the binary left the common envelope. We calculate the period it had when it left the common envelope to be $P_{\text{CE}} = 4.24$ h. Following the same method as in Zorotovic et al. (2010) and based on their results we reconstructed the initial parameters of the binary using a common-envelope efficiency of $\alpha_{\text{CE}} = 0.25$ and the same fraction of recombination energy (see Zorotovic et al. 2010, for more details). We found an initial mass of $M_{\text{prog}} = 1.33 M_{\odot}$ for the progenitor of the WD, which filled its Roche lobe when its radius was $R_{\text{prog}} = 91.3 R_{\odot}$. At that point, the orbital separation was $a = 162.7 R_{\odot}$, and the age of the system was $t_{\text{sys}} = 4.4$ Gyr, since the time it was formed. Using the radius of the secondary⁵ we calculate that the system will reach a semidetached configuration and become a cataclysmic variable (CV) at an orbital period of $P_{\text{sd}} \sim 2$ h in $t_{\text{sd}} = 1.5$ Gyr.

Given that the current P_{orb} places SDSS 1210 right at the upper edge of the CV orbital period gap,⁶ and that the calculated P_{sd} , when SDSS 1210 will start mass transfer, is right at the lower edge of the period gap, we are tempted to speculate whether SDSS 1210 is in fact a detached CV entering (or just having entered) the period gap. Davis et al. (2008) have shown that a large number of detached WD+MS binaries with orbital periods between 2 and 3 h are in fact CVs that have switched off mass transfer and are crossing the period gap. This could in principle explain the apparently oversized secondary in SDSS 1210, as expected from the disrupted magnetic braking theory (e.g. Rappaport, Verbunt & Joss 1983). However, the temperature of the WD in SDSS 1210 seems to be uncomfortably low for a WD that has recently stopped accreting (Townsend & Gänsicke 2009).

9 DISCUSSION AND CONCLUSIONS

In this paper, we have identified SDSS 1210 as an eclipsing PCEB containing a very cool, low-mass, DAZ WD and a low-mass MS companion.

Using combined constraints from spectroscopic and photometric observations we have managed to measure the fundamental stellar parameters of the binary components. Systematic uncertainties in the absolute calibration of our photometric data influence the determination of the stellar radii. The stellar masses, however, remain unaffected and were measured to a 1 per cent accuracy. The (formal) statistical uncertainties in all binary parameters indicate the level of precision that can be achieved in this system. All parameters are summarized in Table 5.

With a mass of $M_{\text{WD}} = 0.415 \pm 0.010 M_{\odot}$ and a temperature of $T_{\text{eff,WD}} \sim 6000$ K, the DAZ WD in SDSS 1210 pushes the boundaries in a hitherto unexplored region of the WD parameter space. The M – R results from the four chains C1 and C2 are consistent with a He-core WD, assuming a hydrogen layer of $M(\text{H})/M_{\text{WD}} = 3 \times 10^{-4}$. However, due to lack of observational constraints for the H-layer

⁵ We assume a representative value of $R_{\text{sec,vol.aver.}} = 0.2 R_{\odot}$ for the volume-averaged radius of the secondary.

⁶ The orbital period range where only a small number of CVs are found.

Table 5. Adopted stellar and binary parameters for SDSS 1210.

Parameter	Value
P_{orb} (d)	0.124 489 764(1)
q	0.379 ± 0.009
a (R_{\odot})	0.870 ± 0.008
Inclination ($^{\circ}$)	$(79.05\text{--}79.36) \pm 0.15$
M_{WD} (M_{\odot})	0.415 ± 0.010
R_{WD} (R_{\odot})	$(0.0157\text{--}0.0161) \pm 0.0003$
$\log g$	7.65 ± 0.02
$T_{\text{eff,WD}}$ (K)	6000 ± 200
K_{WD} (km s^{-1})	95.3 ± 2.1
M_{sec} (M_{\odot})	0.158 ± 0.006
R_{sec} (R_{\odot})	$(0.210\text{--}0.217) \pm 0.003$
$R_{\text{sec,vol.aver.}}$ (R_{\odot})	$(0.197\text{--}0.203) \pm 0.003$
K_{sec} (km s^{-1})	251.7 ± 2.0

thickness and the uncertainty in the radii, we will defer identifying the WD as a definite He core and simply emphasize the strong candidacy.

The secondary star, with a mass of $M_{\text{sec}} = 0.158 \pm 0.006 M_{\odot}$, illustrates once more the excellent opportunity that PCEBs give us for testing and calibrating the M – R relations of low-mass stars. Taking the radius measurements at face value, the secondary star seems to be ~ 10 per cent larger than the theoretical values, although this drops to ~ 5 per cent, if magnetic activity is taken into consideration. In this context, the magnetic activity present in the secondary can lead to the formation of stellar (dark) spots on the surface. The effect of these spots is to block the outgoing heat flux, reducing T_{eff} and, as a result, the secondary expands to maintain thermal equilibrium (Chabrier, Gallardo & Baraffe 2007; Morales et al. 2010). A further ~ 2 per cent inflation could be attributed to tidal and rotational deformation (Sirotkin & Kim 2010; see also Knigge, Baraffe & Patterson 2011). Kraus et al. (2011) found that low-mass stars in short-period binaries appear to be overinflated (although their analysis was restricted to $M_{\text{sec}} > 0.3 M_{\odot}$), which seems to be the case for SDSS 1210. We should note, however, that the mass and radius of the secondary star in the eclipsing PCEB NN Ser (with $M_{\text{sec}} = 0.111 \pm 0.004 M_{\odot}$ and comparable orbital period to SDSS 1210) are consistent with theoretical M – R predictions, even though it is heavily irradiated by the hot WD primary (Parsons et al. 2010a).

We have speculated whether SDSS 1210 is in fact a detached CV entering the period gap, which could explain the large radius of the secondary. This hypothesis could be tested by measuring the rotational velocity of the WD. This can be achieved through high-resolution spectroscopy of the Fe I absorption lines in the WD photosphere (see e.g. Tappert et al. 2011).

In any case, it is highly desirable to improve the measurement of the stellar radii in SDSS 1210 to the comparable precision to the masses presented here. This will require high-precision photometry in standard filters, such as e.g. delivered by ULTRACAM (Dhillon et al. 2007).

ACKNOWLEDGMENTS

We thank the anonymous referee for a prompt report. BTG, TRM, EB and CMC are supported by an STFC Rolling Grant. MRS and AR-M acknowledge financial support from FONDECYT in the form of grants 1100782 and 3110049. MZ acknowledges support from Gemini/CONICYT (grant 32100026). Based in part on

observations made with the William Herschel Telescope operated on the island of La Palma by the Isaac Newton Group in the Spanish Observatorio del Roque de los Muchachos of the Instituto de Astrofísica de Canarias and on observations made with the Liverpool Telescope operated on the island of La Palma by Liverpool John Moores University in the Spanish Observatorio del Roque de los Muchachos of the Instituto de Astrofísica de Canarias with financial support from the UK Science and Technology Facilities Council.

REFERENCES

- Abazajian K. N. et al., 2009, *ApJS*, 182, 543
 Adelman-McCarthy J. K. et al., 2008, *ApJS*, 175, 297
 Althaus L. G., Benvenuto O. G., 1997, *ApJ*, 477, 313
 Andersen J., 1991, *ARA&A*, 3, 91
 Baraffe I., Chabrier G., Allard F., Hauschildt P. H., 1998, *A&A*, 337, 403
 Bayless A. J., Orosz J. A., 2006, *ApJ*, 651, 1155
 Beatty T. G. et al., 2007, *ApJ*, 663, 573
 Berger D. H. et al., 2006, *ApJ*, 644, 475
 Bertin E., Arnouts S., 1996, *A&AS*, 117, 393
 Brown W. R., Kilic M., Hermes J. J., Allende Prieto C., Kenyon S. J., Winget D. E., 2011, *ApJ*, 737, 23
 Çakırlı Ö., Ibanoglu C., 2010, *MNRAS*, 401, 1141
 Casewell S. L., Dobbie P. D., Napiwotzki R., Burleigh M. R., Barstow M. A., Jameson R. F., 2009, *MNRAS*, 395, 1795
 Chabrier G., Gallardo J., Baraffe I., 2007, *A&A*, 472, L17
 Claret A., Bloemen S., 2011, *A&A*, 529, A75
 Copperwheat C. M., Marsh T. R., Dhillon V. S., Littlefair S. P., Hickman R., Gänsicke B. T., Southworth J., 2010, *MNRAS*, 402, 1824
 Davis P. J., Kolb U., Willems B., Gänsicke B. T., 2008, *MNRAS*, 389, 1563
 Debes J. H., 2006, *ApJ*, 652, 636
 Dhillon V. S. et al., 2007, *MNRAS*, 378, 825
 Dimitrov D. P., Kjurkchieva D. P., 2010, *MNRAS*, 406, 2559
 Drake A. J. et al., 2010, preprint (arXiv:1009.3048)
 Dupuis J., Fontaine G., Pelletier C., Wesemael F., 1993, *ApJS*, 84, 73
 Ford E. B., 2006, *ApJ*, 642, 505
 Gänsicke B. T., Araujo-Betancor S., Hagen H.-J., Harlaftis E. T., Kitsionas S., Dreizler S., Engels D., 2004, *A&A*, 418, 265
 Horne K., 1986, *PASP*, 98, 609
 Irwin J. et al., 2010, *ApJ*, 718, 1353
 Knigge C., Baraffe I., Patterson J., 2011, *ApJS*, 194, 28
 Koester D., 2010, *Mem. Soc. Astron. Ital.*, 81, 921
 Koester D., Wilken D., 2006, *A&A*, 453, 1051
 Kraus A. L., Tucker R. A., Thompson M. I., Craine E. R., Hillenbrand L. A., 2011, *ApJ*, 728, 48
 López-Morales M., 2007, *ApJ*, 660, 732
 Marsh T. R., 1989, *PASP*, 101, 1032
 Morales J. C., Ribas I., Jordi C., 2008, *A&A*, 478, 507
 Morales J. C. et al., 2009, *ApJ*, 691, 1400
 Morales J. C., Gallardo J., Ribas I., Jordi C., Baraffe I., Chabrier G., 2010, *ApJ*, 718, 502
 Morrissey P. et al., 2007, *ApJS*, 173, 682
 Nebot Gómez-Morán A. et al., 2009, *A&A*, 495, 561
 Nordhaus J., Spiegel D. S., Ibgui L., Goodman J., Burrows A., 2010, *MNRAS*, 408, 631
 Paczynski B., 1976, in Eggleton P., Mitton S., Whelan J., eds, *Proc. IAU Symp. 73, Structure and Evolution of Close Binary Systems*. Reidel, Dordrecht, p. 75
 Panei J. A., Althaus L. G., Benvenuto O. G., 2000, *A&A*, 353, 970
 Parsons S. G., Marsh T. R., Copperwheat C. M., Dhillon V. S., Littlefair S. P., Gänsicke B. T., Hickman R., 2010a, *MNRAS*, 402, 2591
 Parsons S. G. et al., 2010b, *MNRAS*, 407, 2362
 Parsons S. G., Marsh T. R., Gänsicke B. T., Drake A. J., Koester D., 2011, *ApJ*, 735, L30
 Press W. H., 2002, *Numerical Recipes in C++: The Art of Scientific Computing*. Cambridge Univ. Press, Cambridge
 Press W. H., Teukolsky A. A., Vetterling W. T., Flannery B. P., 2007, *Numerical Recipes. The Art of Scientific Computing*, 3rd edn. Cambridge Univ. Press, Cambridge
 Provencal J. L., Shipman H. L., Hog E., Thejll P., 1998, *ApJ*, 494, 759
 Provencal J. L., Shipman H. L., Koester D., Wesemael F., Bergeron P., 2002, *ApJ*, 568, 324
 Pyrzas S. et al., 2009, *MNRAS*, 394, 978
 Rappaport S., Verbunt F., Joss P. C., 1983, *ApJ*, 275, 713
 Rebassa-Mansergas A., Gänsicke B. T., Schreiber M. R., Koester D., Rodríguez-Gil P., 2010, *MNRAS*, 402, 620
 Rebassa-Mansergas A., Nebot Gómez-Morán A., Schreiber M. R., Girven J., Gänsicke B. T., 2011, *MNRAS*, 413, 1121
 Ribas I., 2006, *Ap&SS*, 304, 89
 Roberts G. O., Gelman A., Gilks W. R., 1997, *Ann. Applied Probability*, 7, 110
 Schreiber M. R., Gänsicke B. T., 2003, *A&A*, 406, 305
 Schreiber M. R., Gänsicke B. T., Southworth J., Schwöpe A. D., Koester D., 2008, *A&A*, 484, 441
 Sirotkin F. V., Kim W.-T., 2010, *ApJ*, 721, 1356
 Southworth J., Clausen J. V., 2007, *A&A*, 461, 1077
 Steele I. A. et al., 2004, *Proc. SPIE*, 5489, 679
 Steele I. A., Bates S. D., Gibson N., Keenan F., Meaburn J., Mottram C. J., Pollacco D., Todd I., 2008, in McLean I. S., Casali M. M., eds, *Proc. SPIE Vol. 7014, Ground-based and Airborne Instrumentation for Astronomy II*. SPIE, Bellingham, p. 217
 Steinfadt J. D. R., Kaplan D. L., Shporer A., Bildsten L., Howell S. B., 2010, *ApJ*, 716, L146
 Tappert C., Gänsicke B. T., Schmidtobreick L., Aungwerojwit A., Mennickent R. E., Koester D., 2007, *A&A*, 474, 205
 Tappert C., Gänsicke B. T., Schmidtobreick L., Ribeiro T., 2011, *A&A*, 523, 129
 Torres G., 2007, *ApJ*, 671, L65
 Townsley D. M., Gänsicke B. T., 2009, *ApJ*, 693, 1007
 Verbunt F., Rappaport S., 1988, *ApJ*, 332, 193
 Verbunt F., Zwaan C., 1981, *A&A*, 100, L7
 Webbink R. F., 2008, in Milone E. F., Leahy D. A., Hobill D. W., eds, *Astrophys. Space Sci. Library*, Vol. 352, *Short-Period Binary Stars: Observations, Analyses and Results*. Springer, Berlin, p. 233
 Wood M. A., 1995, in Koester D., Werner K., eds, *Lecture Notes in Physics*, Vol. 443, *White Dwarfs*. Springer-Verlag, Berlin, p. 41
 York D. G. et al., 2000, *AJ*, 120, 1579
 Zorotovic M., Schreiber M. R., Gänsicke B. T., Nebot Gómez-Morán A., 2010, *A&A*, 520, A86
 Zuckerman B., Koester D., Reid I. N., Hünsch M., 2003, *ApJ*, 596, 477

This paper has been typeset from a $\text{\TeX}/\text{\LaTeX}$ file prepared by the author.